1 # Revealing importance of particles' surface functionalization on the properties of
2 # magnetic alginate hydrogels

3

4 Mariusz Barczak[1*], Piotr Borowski[1], Cristina Gila-Vilchez[2,4], Miguel Alaminos[3,4], Fernando González-

5 Caballero[2,4], Modesto T. López-López[2,4*]

6 [1] Department of Theoretical Chemistry, Institute of Chemical Sciences, Faculty of Chemistry,

7 Maria Curie-Skłodowska University, 20031 Lublin, Poland

8 [2] Department of Applied Physics, Faculty of Sciences, University of Granada, 18071 Granada, Spain

9 [3] Tissue Engineering Group, Department of Histology, University of Granada, Granada, Spain

10 [4] Instituto de Investigación Biosanitaria ibs.GRANADA, Granada, Spain

11 *Corresponding authors: M.B.: mbarczak@umcs.pl, M.T. L.-L.: modesto@ugr.es*

12

13 **Abstract:**

14 Iron/silica core-shell microparticles (IMPs) were functionalized by different functional groups

15 including amine, glycidoxy, phenyl, and thiocyanate. Many of the IMPs modifications are reported for the

16 first time. The resulting surface chemistry turned out to affect the properties of magnetic alginate

17 hydrogels fabricated from sodium alginate and dispersed IMPs. Differences in magnetorheological

18 properties of the obtained magnetic hydrogels can be at least partially attributed to the interactions

19 between alginate and surface functionalities of IMPs. Density Functional Theory (DFT) calculations were

20 carried out to get detailed insight into those interactions in order to link them with the observed

21 macroscopic properties of the obtained hydrogels. For example, amine groups on the IMPs surface

22 resulted in well-formed hydrogels while the presence of thiocyanate or phenyl groups – in poorly formed

23 ones. This observation can be used for tuning the properties of various carbohydrate-based hydrogels.

24

25 **1. Introduction:**

26 Hydrogels can be considered as three-dimensional, hydrophilic networks of flexible polymer chains

27 swollen by water or other fluid. They are able to store a large amount of water (even up to thousands

28 times their dry weight) while maintaining the structure that can be cast into practically any shape or

29 form (Seliktar, 2012). They are soft and capable of retaining large amounts of water thus closely

30 resemble living tissues. Mainly for that reason hydrogels are considered as particularly promising

31 materials in the rapidly developing field of tissue engineering as matrices for replacing and regenerating

32 different tissues and organs (Drury & Mooney, 2003; Geckil, Xu, Zhang, Moon, & Demirci, 2010; Peppas,

33 Hilt, Khademhosseini, & Langer, 2006). Besides they also continuously find widespread applications in

34 the biomedical field including biosensors (Buenger, Topuz, & Groll, 2012; L. Li et al., 2015; Ulijn et al.,

35 2007), drug delivery systems (Fan, Tian, & Liu, 2019; J. Li & Mooney, 2016; Qiu & Park) or wound healing

36 materials (Dimatteo, Darling, & Segura, 2018; Griffin, Weaver, Scumpia, Di Carlo, & Segura, 2015; Liu &

37 Guo, 2018).

38   There is a plethora of different hydrogelators which can be used to fabricate hydrogels. Depending

39 on hydrogelator origin, the resulting hydrogels can be: (i) natural polymer-based hydrogels, (ii) synthetic

40 polymer-based hydrogels and (iii) supramolecular hydrogels (Du, Zhou, Shi, & Xu, 2015). Natural

41 polymer-based hydrogels are particularly useful in tissue engineering related applications due to their

42 remarkable *in vitro* and *in vivo* biocompatibility, confirmed in many studies (De Groot et al., 2001;

43 Kulkarni, Boppana, Krishna Mohan, Mutalik, & Kalyane, 2012; Lai, 2010; C. Lee et al., 2013). Indeed, in

44 the literature there is a continuously increasing number of papers reporting such potential biomedical

45 applications with the use of alginate, chitosan, fibrin or collagen as the most prominent examples of

46 natural polymer-based hydrogels; many recent reviews nicely summarize the current state-of-the-art

47 (Dimatteo et al., 2018; X. Li, Sun, Li, Kawazoe, & Chen, 2018; Mahinroosta, Jomeh Farsangi, Allahverdi, &

48 Shakoori, 2018; Mantha et al., 2019; Qureshi et al., 2019; Tu et al., 2019).

49   Among different hydrogels' types, alginate-based hydrogels are considered as one of the preferred

50 formulations, mainly due to low cost and excellent biocompatibility of alginate hydrogelators (Espona-

51 Noguera et al., 2018; Soon-Shiong et al., 1994; Wang et al., 2019). Alginates (i.e., sodium, potassium,

52 calcium or magnesium salts of alginic acid) are biopolymers usually extracted from different species of

53 seaweeds (macroalgae) such as, for example, *Rhodophyceae* (red macroalgae), *Phaeophyceae* and

54 *Laminaria* (brown macroalgae) or *Chlorophyceae* (green macroalgae). From chemical point of view

55 alginic acid is composed of unbranched chains of α-*L*-guluronic acid (G-block) and β-*D*-mannuronic acid

56 (M-block) covalently linked by 1-4 glycosidic bond (Fig. S1). Alginates extracted from different species

57 usually show variations in their chemical structure due to different sequences of G- and M-blocks (K. Y.

58 Lee & Mooney, 2012). In the presence of multivalent cations (e.g., calcium) alginates form a physical

59 ionotropic hydrogel as a result of ionic crosslinking between the negatively charged polyionic alginate

60 chains and multivalent cations. Negative charge of the alginate chains results from dissociation of –COOH

61 (alginic acid) or –COONa (alginate) groups into carboxylate anions –COO$^-$.

62   To fabricate "smart" materials, alginate hydrogels can be doped with magnetic particles.

63 Incorporation of magnetically-susceptible species into hydrogel structure may provide additional

64 features like stimuli-responsive action, sufficient biocompatibility or tailorable rheological properties
65 (Gila-Vilchez, Duran, Gonzalez-Caballero, Zubarev, & Lopez-Lopez, 2019; Konwar, Gogoi, & Chowdhury,
66 2015; Supramaniam, Adnan, Mohd Kaus, & Bushra, 2018). For those reasons, magnetic hydrogels are
67 becoming even more useful for biomedical applications, particularly as scaffolds for soft tissue
68 engineering, where the above-mentioned advantages are of paramount importance. The rheological
69 properties of the magnetic hydrogels (also called ferrogels) in the presence of magnetic field are then
70 predominantly controlled by the factors related to the type, size, shape and concentration of the
71 incorporated magnetic particles (Bonhome-Espinosa et al., 2017; Gila-Vilchez et al., 2018; Gila-Vilchez,
72 Duran, et al., 2019; Gila-Vilchez, Mañas-Torres, et al., 2019). For example, small particles (e.g.,
73 nanoparticles) experience a weak attraction between themselves under moderate magnetic field in
74 contrast to bigger particles (e.g., microparticles) which are able to interact strongly even at low magnetic
75 fields. Thus strong magnetic fields can provoke significant viscoelasticity changes of magnetic hydrogels
76 composed of microparticles (Gila-Vilchez et al., 2018). The fascinating research area of magnetic
77 hydrogels is, however, still at its infancy. There is a considerable number of reports about ferrogels but
78 they do not fully reflect the high potential they have with regard to the current and emerging biomedical
79 challenges.

80 Functionalized magnetic particles can be used to modulate the interactions between them and the
81 polymer filaments that form the hydrogels having a direct impact on the properties of the hydrogels, as
82 has been recently shown (Bonhome-Espinosa et al., 2017). Furthermore, magnetic particles with the
83 appropriate surface chemistry can conjugate drugs, proteins, enzymes or antibodies, which is required
84 for numerous applications. For instance, it has been recently shown that medical treatment with
85 magnetic particles conjugated by nerve growth factor significantly promotes neurite outgrowth and
86 increases the complexity of the neuronal branching trees (Marcus, Skaat, Alon, Margel, & Shefi, 2015).

87 As can be seen from the comprehensive set of representative literature presented above the
88 magnetic particles are usually used as received, i.e., without any functionalization. Incorporation of
89 nano- or micro-sized particles into hydrogel is based on the physical incorporation within the hydrogel,
90 having the possible consequence of continuous release of the particles from the hydrogel matrix to the
91 environment (Barbucci, Giani, Fedi, Bottari, & Casolaro, 2012). However, apart from bulk iron providing
92 magnetic field actuation, the surface of magnetic particles can be used to tune specific or nonspecific
93 interactions with the hydrogelator moieties (Tanasa et al., 2019), which in turn can affect the final
94 properties of resulting hydrogels and even provide more favorable features like better adhesion of
95 biological species (e.g., cells). Functionalization with amine group with the use of 3-

96   aminopropyltriethoxysilane or 3-aminopropyltrimethoxysilane is frequently reported strategy to modify

97   the surface of the particles and properties of resulting hydrogels (Barbucci et al., 2012; Čampelj,

98   Makovec, & Drofenik, 2009; Giani, Fedi, & Barbucci, 2012; Long et al., 2015; Park et al., 2009; Zhu, Zheng,

99   Wang, & Wang, 2016). Unfortunately, in the literature there is few attempts to chemically functionalize

100   magnetic particles using groups other than amines (Tanasa et al., 2019).

101   In this work we seek to determine the role of surface functionalization of iron particles on the

102   properties of the resulting alginate magnetic hydrogels. We hypothesize that different surface

103   chemistries of iron particles can affect chemical interactions between the both phases in a distinct way,

104   and these changes will contribute to the different microstructure, mechanical properties, and

105   biocompatibility of ferrogels. Alginate was chosen as a model matrix due to its high biocompatibility

106   allowing its use in biomedical applications. A set of different surface functionalizations of iron/silica core-

107   shell microparticles (IMPs) has been chosen. Interactions between specific surface groups and alginate

108   chains have been elucidated with the aid of DFT quantum chemistry calculations to get a more detailed

109   insight into those interactions.

110

111   **2. Experimental**

112   *2.1. Reagents*

113   Sodium alginate (ALG, MW: 20-40 kDa, Sigma Aldrich) was used as received. The relative content of

114   mannuronic to guluronic acid was experimentally estimated using protocols based on ellipsometry

115   (Donati et al., 2003; Morris, Rees, & Thom, 1980) and FTIR spectroscopy (Filippov & Kohn, 1974). The

116   ellipsometric method showed that the composition of ALG is as follows: 75% guluronic acid, 17%

117   mannuronic acid, and 8% mixed sequences (cf. Fig. S1b); while FTIR method showed that it is: 82%

118   guluronic acid and 18% mannuronic acid (cf. Fig. S1c). Powder of sodium alginate, as received, had a bulk

119   density of 0.509 ± 0.017 g/mL and the reported skeleton density of sodium alginate is 1.6010 ± 0.0002

120   g/mL (Censi, Gigliobianco, Malaj, & Di Martino, 2016). From this data, we estimated a porosity of the

121   sodium alginate powder of 68.2 ± 1.1 % - for details on the bulk and skeletal density of aerogels see

122   (Fitzpatrick, Staiger, Deb-Choudhury, & Ranford, 2018). Calcium carbonate ($CaCO_3$, Sigma Aldrich), D-

123   glucono-δ-lactone (GDL, Sigma Aldrich), aminopropyltriethoxysilane (APTES, 97%, Sigma-Aldrich), (3-

124   trimethoxysilylpropyl)diethylenetriamine   (TMPMT,   95%,   Fluorochem),   N-

125   phenylaminomethyltriethoxysilane (PATES, 95%, Fluorochem), thiocyanatopropyltriethoxysilane (TCTES,

126   95%, Fluorochem), glycidoxypropyltrimethoxysilane (GPTMS, 98%, Sigma Aldrich), phenyltriethoxysilane

127   (PTES, 97%, Gelest), sodium hydroxide (NaOH, Sigal), hydrochloric acid (HCl, Sigal) were used without

128   further purification. As magnetic particles we used silica-covered iron particles (CIP grade) supplied by

129   BASF, Germany, referred in the test as IMPs.

130   *2.2. Functionalization of iron/silica core-shell microparticles*

131   2 g of IMPs were placed in a vial and mixed with 40 mL of absolute ethanol, previously acidified with 0.57

132   mL of 1.75 M HCl. The suspension was sonicated for 5 min. After that time 1 mmol of proper

133   organofunctional alkoxysilane (APTES, TMPMT, PTES, GPTMS, PATES or TCTES) was added and the

134   suspension was submitted six times to the following sequence: 5 min of sonification and 25 min of

135   stirring (in total 3 hours). After that time the IMPs were separated from the solution by magnet, washed

136   two times with absolute ethanol and dried overnight at 40 °C. The numbering of the samples together

137   with the organofunctional alkoxysilane used to their synthesis is given in Table 1.

138   *2.3. Preparation of magnetic hydrogels*

139   For the preparation of the magnetic hydrogels we followed a two-step protocol proposed in a previous

140   work (Gila-Vilchez et al., 2018), which allows the generation of magnetic hydrogels with excellent

141   homogeneity and reproducibility. Briefly, ALG was dissolved in distilled water to prepare 1% w/v

142   solution. Then, 9 mg of $CaCO_3$ was added to 6 mL of this solution, and the vial was vortexed for 1 min.

143   After that 32 mg of GDL was added and the mixture was again vortexed for 1 min. Then the solution was

144   left in a closed vial for 90 min at room temperature. After that time the forming gelling mixture was

145   transferred to another vial, vortexed (1 min) and 0.7 mL was transferred do the Eppendorf vial

146   containing specific amount of IMPs to reach the required final concentration of 0.9% v/v *(note that from*

147   *the initial amount of ALG mixture of 6 mL it is possible to prepare more IMP-ALG hydrogel samples of 0.7*

148   *mL).* The mixture of gel and IMPs in the Eppendorf vial was submitted to the following treatment steps to

149   disperse well the IMPs within the gel: (i) vortex - 1 min, (ii) sonification - 5 min, (iii) vortex - 1 min. After

150   this sequence the gel was transferred to the open vial and kept overnight in a water-saturated

151   atmosphere. The next day the formed hydrogels were submitted to the further analyses. In the case of

152   the non-magnetic reference hydrogel the preparation scheme was the same apart from the fact that 0.7

153   mL of the solution was transferred to the empty Eppendorf vial without IMPs.

154   *2.4. Physicochemical characterization of the IMPs*

155   IMPs were analyzed by several instrumental techniques. The nitrogen sorption measurements were

156   performed at −196 °C using a 1200e sorption analyzer (Quantachrome). All samples were degassed at

157   110 °C in vacuum prior to measurements. The BET specific surface areas (S_{BET}) were evaluated in the

158   range of relative pressures of 0.05–0.20. The total pore volumes (V_p) were calculated by converting the

159   amount of adsorbed nitrogen at relative pressure ∼0.99 to the volume of liquid adsorbate. The SEM

160   imaging of randomly selected parts of the surface was performed under high vacuum conditions by

161   means of Quanta 3DFEG (FEI, USA) microscope with the accelerating voltage 5/20 kV. X-ray

162   photoelectron spectroscopy (XPS) spectra were obtained in high vacuum (8×10^{-9} Pa) by means of Multi-

163   Chamber Analytical System (Prevac, Poland) equipped with monochromatic 450 W Al K-alpha X-ray

164   radiation source. The binding energy scale was referenced against C 1s = 284.7 eV line. Deconvolutions of

165   the obtained spectra were done using MultiPak software. To determine the surface pH 0.1 g of IMPs was

166   suspended in 50 mL of water and stabilized overnight before the measurement. The pH of the solution

167   was then measured using a 510 pH-meter (Oakton Instruments). The zeta potential was evaluated using

168   Zetasizer Nano ZS (Malvern Instruments). Suspensions were prepared by dispersing ~5 mg of IMPs in

169   2 mL of 1×10^{-3} M KCl.

170   *2.5. Physicochemical characterization of the IMPs-ALG hydrogels*

171   The water-releasing tests were carried out for each hydrogel (in triplicate). Fresh hydrogel with known

172   mass (~0.47-0.51 g) was placed in a plastic vial and submitted to drying at room temperature. Weight

173   losses were recorded during drying at specific times during 14 hours (i.e., until the bottom of the vial

174   only dry residue remained and the weight did not change over time). Humidity was not controlled during

175   the experiments but it was the same for all the samples. The microscopic structure of the selected

176   hydrogels was analyzed by Scanning Electron Microscopy (SEM), accomplished using a FEI Quanta 400

177   ESEM equipped with a Peltier effect cooling stage. Before SEM analysis, the hydrogels were prepared

178   according to a well-established protocol (detailed information is provided in Supplementary data) and

179   subjected to CO_2 critical point drying (Anderson, 1951). Differential scanning calorimetric (DSC)

180   measurements were carried out using a DSC 204 Netzsch calorimeter. The dynamic mode scans were

181   collected at a heating rate of 20 °C·min^{-1}, from 20 °C to 200 °C under argon flow (20 cm^3·min^{-1}).

182   Aluminum pots were punched with a needle before each experiment.

183   *2.6. Rheological measurements of the IMPs-ALG hydrogels*

184   Rheological properties of the hydrogels were determined at room temperature using the MCR 300

185   magneto rheometer (Physica Anton Paar) using a plate-plate geometry of 20 mm of diameter. Linear

186   viscoelastic region (LVR) of the studied hydrogels was determined by subjecting them to deformation

187   amplitude sweep tests at a constant frequency of 1 Hz and stepwise increasing shear strain amplitude,

188   γ_0. From these measurements the values of the storage (G') and loss (G'') moduli as a function of γ_0 were

189   determined along with the averaged G' and G'' values within the LVR region. Frequency sweep tests

190   were done at a fixed shear strain amplitude (γ_0=0.03%) within the LVR, and increasing frequency in the

191   range from 0.15 to 15 Hz. From these measurements the values of G' and G'' were determined as

192   functions of frequency. Both amplitude and frequency scans were carried without and with the presence

193   of magnetic field of two arbitrarily chosen intensities of 141 kA m^{-1} and 242 kA m^{-1}.

194   *2.6. Cell viability assessment*

195   First, the viability of the human fibroblasts was analyzed using functional WST-1 assays (Cell

196   Proliferation Reagent WST-1, Roche Diagnostics, Germany) based on the colorimetric transformation of

197   tetrazolium salt (WST-1) to formazan driven by the activity of the mitochondrial dehydrogenase of living

198   cells, which is directly proportional to the number of viable (i.e., metabolically active) cells. Fibroblasts

199   were cultured for 48 h in contact with hydrogel, and the absorbance of the colorimetric reaction was

200   inspected with an Assay UVM 340 spectrophotometer in triplicate.

201   To determine the structural integrity of cells cultured in contact with the biomaterials, the total

202   DNA released by the cells corresponding to each condition was quantified with a NanoDrop 2000 UV-Vis

203   Spectrophotometer (Thermo Fisher Scientific). 10 µL of the culture medium was used to determine the

204   amount of DNA for each condition and time. The release of DNA from cells into the culture medium

205   occurs as a result of irreversible damage to the cell membrane. Therefore higher DNA concentration in

206   the culture medium indicates a higher number of dead cells with the membrane structurally disrupted.

207   Finally, Live/Dead cell viability assays were used on cell cultured with the different types of

208   materials evaluated in the present work. This method combines a functional assay based on calcein AM,

209   which is metabolically activated and turns to green by living cells, and a structural assay based on

210   ethidium homodimer-1, which can only enter to the cell nucleus if the cell is dead. Therefore, living cells

211   are labeled in green and dead cells are labeled in red. Cells were cultured in the presence of each

212   material for 48 h and washed in PBS. Then, calcein AM and ethidium homodimer-1 were added as

213   suggested by the manufacturer, and representative micrographs were taken from human fibroblasts

214   cultured for 48 h in contact with magnetic hydrogels using an A1R Nikon fluorescence microscope

215   (Nikon) with constant illumination and capture parameters. Micrographs were analyzed using the NIS-

216   Elements and ImageJ v1.46 software packages, and the percentage of live and dead cells was calculated

217   for each experimental condition.

218   *2.7. Theoretical calculations*

219   The Density Functional Theory (DFT) calculations were carried out at the DFT/B3LYP/6-311++G**

220   level. Equilibrium geometries and harmonic vibrational frequencies of the considered molecular systems

221 were found first. The type of stationary point was determined by analysis of the obtained frequencies.
222 All calculated frequencies were real indicating that minima on PES were found. Calculations were
223 performed using the PQS quantum chemistry package (Baker et al., 2009). The relative energies, which
224 include zero-point vibrational energy (ZPVE) corrections, were calculated as ΔE=E(products)-
225 E(substrates), thus the negative value of ΔE means that the products are more stable than substrates.
226 Following our previous findings (Barczak & Borowski, 2019; Barczak, Wierzbicka, & Borowski, 2018) we
227 considered interactions of alginate representative fragments and functionalities as the energetics is not
228 affected by the presence of the matrix.

229 *2.8. Statistical analysis*

230 Parametric analysis of variance (ANOVA) was used to determine differences between hydrogels with
231 respect to their water releasing profiles and storage modulus (G'). After ANOVA analysis, pairwise
232 multiple comparisons analysis was performed using Tukey HSD and Dunnett two-tailed post hoc tests.
233 For Dunnett test, the R hydrogel was a single control. A difference was considered to be statistically
234 significant if p value was lower than 0.05. Hydrogels biocompatibility (i.e. WST-1 and DNA quantification)
235 due to the lack of samples normality (as confirmed by Shapiro-Wilk test), was assessed using non-
236 parametric Kruskal-Wallis test, followed by multiple pairwise comparisons based on the Conover-Iman
237 post host test. A difference was considered statistically significant if the p-value was less than 0.05
238 corrected by Bonferroni correction.

239

240 **3. Results and discussion**

241 *3.1. Functionalization and characterization of iron microparticles*

242   The commercial iron core/shell particles (IMPs) used in this study are composed of spherical and
243 often aggregated units with a wide distribution of sizes. The SEM images of the initial particles (referred
244 as R) at different magnifications are presented in Fig. 1. The average size is around 2-3 μm and the
245 density of 7.71 ± 0.19 g cm^{-3}. The IMPs used in this study exhibit a typical ferromagnetic behavior with
246 saturation magnetization of approx. 1600 kA m^{-1} (Gila-Vilchez et al., 2018). The particles are covered,
247 though not perfectly, with a layer of silica thus there are many surface silanol groups present, which
248 makes the resulting surface very versatile and ready to be modified by attaching specific functional
249 groups. Due to that the grafting of different organosilica monomers was chosen in this study as the most
250 straightforward functionalization strategy. To accomplish it, six different monomers were tested – the
251 range of the monomers used is listed in Table 1; grafted functional groups are also presented in Fig. 1
252 and S2a. The reason for choosing such a wide range of functional groups was twofold: (i) examining

253   whether functionalization of iron surface can be achieved using monomers other than APTES and (ii)

254   investigating the possible effect of chemistry of IMP surface layer on the properties of obtained alginate

255   magnetic hydrogels. The choice of functional groups used in this study was dictated by the fact that they

256   can interact with the alginate network in various ways. For example, amino or thiocyanate groups can

257   form hydrogen bonds with alginate oxygens, while phenyl or glycidoxy groups are expected to

258   repulsively interact with a negatively charged alginate hydrogel network.

259

Table 1. Structural and chemical properties of the functionalized iron particles

No.	Monomer	Grafted functional group	Nitrogen sorption[&]			XPS elemental comp. (at. %)					EDS elemental comp. (at. %)					pH	ζ [$]
			S_{BET} $(m^2 g^{-1})$	V_t $(cm^3 g^{-1})$	d (nm)	Fe	O	C	Si	N	Fe	O	C	Si	N		(mV)
R	---	---	2.3	0.003	6.0	3.7	25.4	68.7	2.2	---	42.6	21.7	34.5	0.4	---	5.8±0.05	~7
1	APTES	I° amine	3.8	0.003	2.9	2.4	23.2	68.6	5.1	---	41.2	17.2	40.6	0.5	---	4.7±0.03	~20
2	TMPMT	I° and II° amine	2.6	0.004	6.0	4.5	34.2	43.7	14.9	2.5	57.8	7.8	31.2	0.4	2.4	5.2±0.03	~20
3	GPTMS	glycydoxy	1.9	0.001	3.4	3.4	25.2	64.9	6.5	---	22.2	40.5	35.9	0.7	---	5.6±0.05	~ 3
4	PTES	phenyl	4.1	0.005	5.1	3.3	24.4	68.1	4.2	---	35.9	29.6	33.4	0.5	---	5.2±0.02	~(-1)
5	PATES	aminophenyl	1.3	0.002	5.2	1.9	24.1	67.3	6.7	---	60.5	7.1	31.8	0.4	---	5.8±0.04	~9
6	TCTES	thiocyanato	19.1	0.014	3.0	6.3	29.4	57.9	6.4	---	52.8	12.9	33.6	0.4	---	6.3±0.07	~3

261 S_{BET} – specific surface area by BET method, V_t – total volumes of the pores, d – average pore size

262 [&] – The error associated with the determination of porous structure parameters based on nitrogen sorption data is usually assumed to be ±2 %. In this case – due to the low

263 porosity – this error can be higher.

264 [$] – IMPs quickly settle on the bottom of the measuring cell preventing accurate measurement of zeta potential, therefore the values given, although averaged over three

265 measurements, should be treated as approximate.

266   The first visual observation is that the color of ethanol solution during the functionalization
267   changes depending on the monomer used (Fig. S2b). This means that the outer silica layer of IMPs is not
268   perfect and the solution containing organosilica monomers can be easily contacted with the carbonyl
269   iron. Due to that some reactions can occur between the carbonyl iron and the organosilica monomers as
270   well as traces of contaminants (note that the purity of the monomers is within the range of 95-97% so
271   some initial reagents/co-products/catalysts are also present). Different colors of the solutions mean that
272   the different sets of reactions may occur. Interestingly, the reference sample R (no organosilica
273   monomer added) changed the color which means that some IMPs have nanometric dimensions and form
274   stable suspension of iron nanoparticles (cf. Fig 2b). Only the sample 2 does not change color what may
275   be explained by fast attachment of the silica monomer due to the presence of reactive methoxy groups.
276   In fact, high content of silica of the sample 2 (*vide infra*) is due to the formation of a tight organosilica
277   layer surrounding the IMPs, which does not allow the reactions, as is the case with other systems.

278   To investigate the effect of functionalization on the structural and chemical properties of the
279   resulting IMPs, they were submitted to thorough characterization by a wide range of instrumental
280   techniques. SEM images of the obtained microparticles are presented in Fig. 1. As can be seen the IMPs
281   are composed of spherical multisized and often agglomerated spheres. After functionalization the
282   particles remain unchanged – the only exception is sample 6, where complex formation/corrosion is
283   observed under higher magnification. Indeed, thiocyanates are considered to be highly corrosive to iron
284   and steel (Melendres, O'Leary, & Solis, 1991; Ravald, Chilver, & Williams, 2007) and they can also form
285   red complexes with iron. The occurring corrosion confirms the fact that the silica coating is not
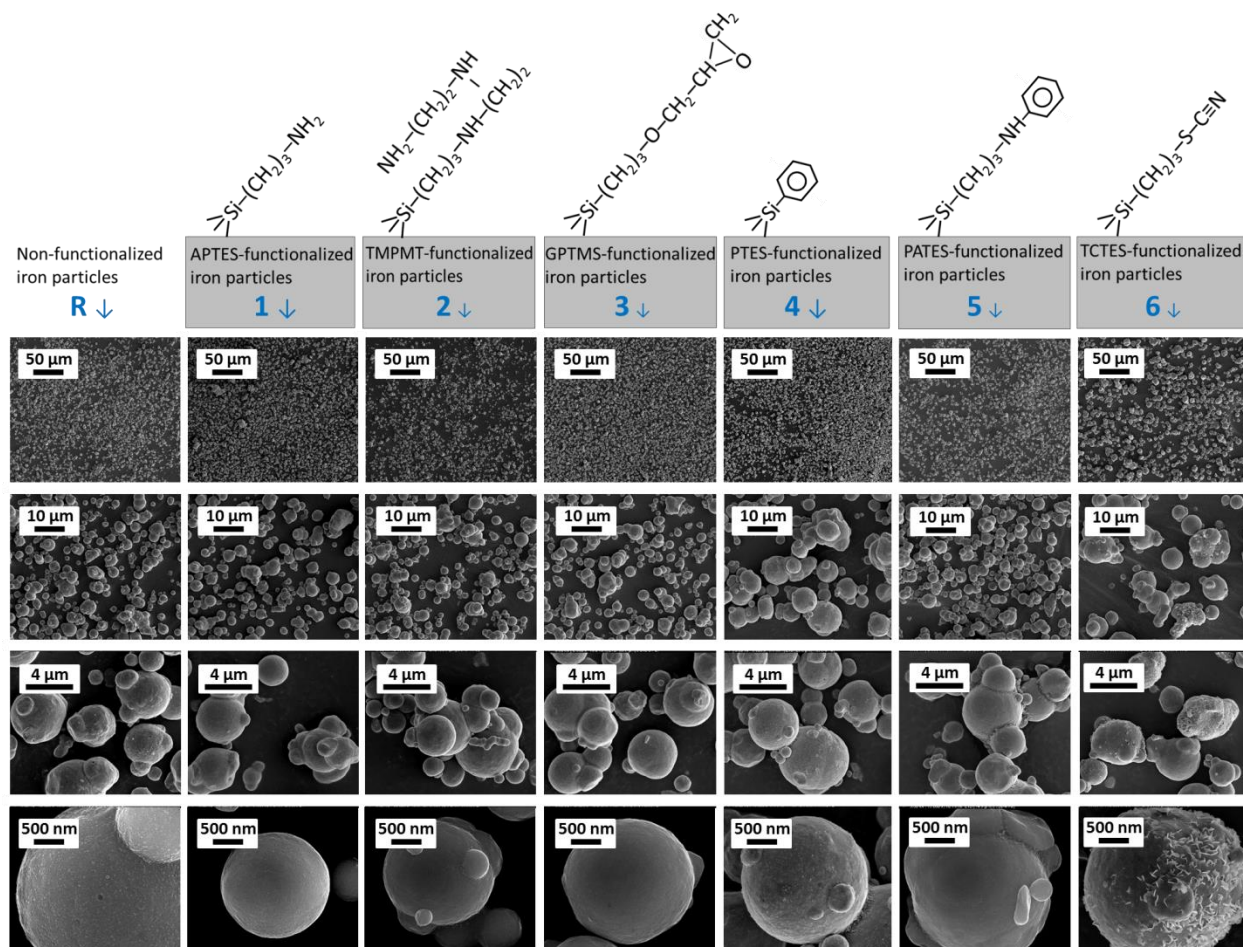286   sufficiently tight to protect the core iron from the contact with external environment.

Fig. 1. SEM microphotographs of the iron microparticles at different magnifications

Structural parameters of the porous structure derived from nitrogen sorption isotherms are given in Table 1. As can be seen all the microparticles but 6 have low specific surface areas (in the range of 1.3-4.1 $m^2 g^{-1}$) and pore volumes (in the range 0.001-0.005 $cm^3 g^{-1}$). Only sample 6 has higher values of S_{BET} and V_p (19.1 $m^2 g^{-1}$ and 0.014 $cm^3 g^{-1}$, respectively), when compared with the rest of the samples, due to remarkable corrosion. The fast corrosion process of the sample 6 was confirmed by visual observation of water solutions of microparticles in closed vials kept for 30 days (cf. Fig. S3). After that time reddish iron oxide layer was formed in the case of 4 (after ~10 days) and 6 (after 1 day) but not in the case of the remaining samples. This clearly testifies that the iron microparticles have different types of the external layers, some of them inhibiting and some of them accelerating corrosion process. From the point of view of biomedical applications the effective inhibition of corrosion is very important due to the permanent contact of iron particles with different physiological fluids. Thus functional groups accelerating corrosion cannot be used in those applications regardless of their functional usefulness.

301   Apart from morphological features also the chemistry of the functionalized magnetic particles was

302   thoroughly inspected by two quantitative methods: XPS and EDS. The first one is considered a surface-

303   sensitive technique enabling determination of the surface composition to a depth up to several nm

304   (Burrell, 2001) while the second - to several hundred nm (Prencipe, Dellasega, Zani, Rizzo, & Passoni,

305   2015). When analyzing data collected in Table 1, the first conclusion is that the results collected using

306   both techniques are significantly different which means that the chemical composition of the surface is

307   different from the chemical composition of the bulk phase. Another general observation from the EDS

308   elemental analysis (which was derived from three different probing regions for each sample) is that the

309   overall chemical composition is extremely variable demonstrating the remarkable chemical

310   heterogeneity (in addition to the structural one as evidenced by SEM analysis). For example looking at

311   the EDS elements content it can be seen that the iron content is in the range 22.2-60.5 %, and oxygen –

312   7.1-40.5 %. The contents of carbon and silicon are more homogenous: 31.2-40.6 % and 0.4-0.7 %,

313   respectively. In the case of the sample 2 functionalized by TMPET significant amount of nitrogen was

314   detected by both, EDS (2.4 %) and XPS (2.5 %).

315   Interestingly, XPS elemental analysis shows that carbon is the more abundant element present on

316   the surface, while the iron content is low. XPS elemental analysis reveals that the silicon content in the

317   initial IMPs is only 2.2 % while after each functionalization it elevates significantly, from 4.2 % (sample 4)

318   to 14.9 % (sample 2). In the case of the latter the functionalization was the most efficient, which is also

319   supported by the fact that the content of nitrogen introduced in the course of functionalization is high

320   (2.4 %). In the case of other samples functionalized by monomers containing amine groups (samples 1

321   and 5), the amounts of nitrogen were apparently below the detection limit of both techniques.

322   The higher efficiency of functionalization with the use of TMPMT than APTES and PATES can be

323   related to three factors. The first factor is that the larger ethoxy groups of APTES and PATES hydrolyse

324   more slowly than smaller methoxy groups of MPTMS (Brochier Salon & Belgacem, 2011; Osterholtz &

325   Pohl, 1992). The second factor is that the amine groups are additionally catalysing the processes of

326   hydrolysis and condensation of TMPMT facilitating the formation of bigger clusters of co-condensed

327   MPTMS molecules which are finally bound to the IMP' surface. The third factor is that metals and many

328   metal oxides can strongly adsorb silanes if a chelating functionality such as diamine is present. The last

329   two factors explain the difference in functionalization efficiency between TMPMT and GPTMS - another

330   methoxy-derived monomer used in this work.

331   The values of surface pH and ζ potential also vary depending on the samples testifying to the

332   remarkable chemical changes of the surface character occurring during functionalisation. In contrast to

333   XPS and EDS techniques which have intrinsic local probing character, ζ potential and surface pH shows

334   overall effect of surface chemistry alterations. As can be seen in the case of the samples 1 and 2 the

335   values of ζ potential significantly shift towards more positive values, most probably due to the presence

336   of protonated amine groups. In contrast, for the sample 4 the value of ζ potential is slightly negative,

337   because of the presence of π electrons of phenyl rings introduced during functionalization. Changes of

338   pH values are more subtle; nevertheless, even those subtle changes show that the surface of magnetic

339   particles is different in each case. For example, lowering of pH from 5.8 for R sample to 4.7, 5.2 and 5.2

340   for the samples 1, 2 and 5, respectively testify to the releasing H_3O^+ ions from the protonated amine

341   groups. Majority of amine groups are protonated because during the functionalization (see Experimental

342   part for details) a small amount of hydrochloric acid was used to catalyze the hydrolysis of alkoxy groups

343   of the silica monomers.

344

345   *3.2. Preparation and structural characterization of magnetic alginate hydrogels*

346   Alginate hydrogels fabricated with the use of non-functionalized and functionalized iron

347   microparticles were first inspected visually (Fig. 2). As can be seen they retained the shape of the

348   container used for their preparation. All ferrogels were black, albeit with different macroscopic

349   appearance: hydrogels 1, 2, and 5 were highly homogeneous, while in the case of the remaining samples,

350   partial separation of water was observed on the next day (cf. Fig. 2: the water envelope around the

351   hydrogels 3 and 4 is clearly visible). In the case of the hydrogel 6 the hydrogel structure was collapsed

352   and the color was changed due to the formation of the red complexes with iron or/and progressing

353   corrosion. Since all the hydrogels were obtained in the same time using the same stock solution of

354   alginate, the resulting changes in the physical appearance are undoubtedly attributed to the different

355   surface chemistries of the incorporated magnetic microparticles. For well-formed hydrogels (samples 1,

356   2 and 5), magnetic microparticles were not only entrapped within the polymer network, but bonded

357   effectively to the alginate chains and consequently, no leakage of magnetic microparticles was observed

358   in these hydrogels (even after immersing samples 1, 2 and 5 in water for several days). On the contrary,

359   as observed in Fig. 2, leakage of particles took place for the other hydrogels.

R-ALG 1-ALG 2-ALG 3-ALG 4-ALG 5-ALG 6-ALG

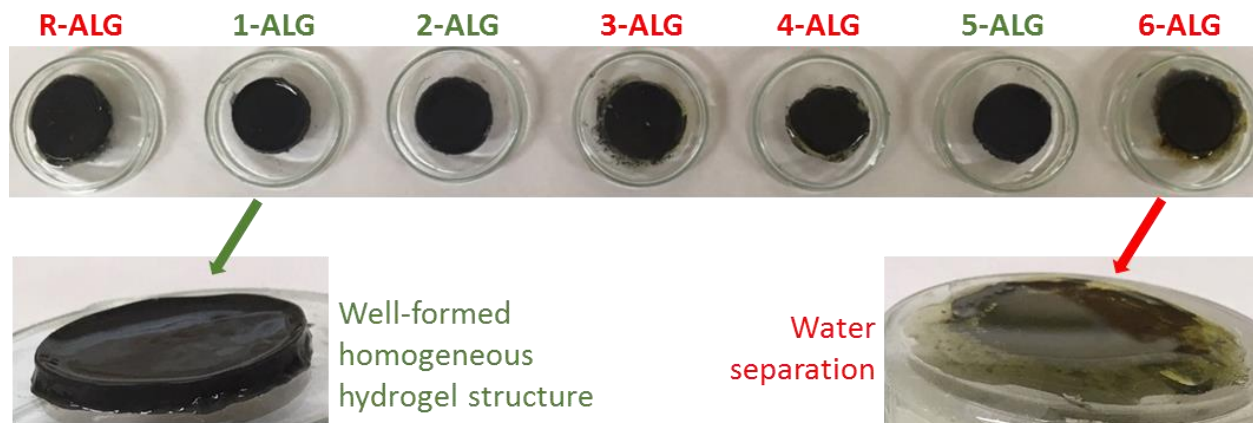Well-formed homogeneous hydrogel structure

Water separation

Fig. 2. Physical appearance of magnetic hydrogels studied. Note that in the case of the hydrogels 3, 4 and 6 a liquid phase separated from the bulk hydrogel structure is seen

The water-releasing behavior of the magnetic hydrogels at room temperature is presented in Fig. 3a. For non-magnetic alginate hydrogel, A, the total weight loss was 98.4% while for the magnetic hydrogels the total weight losses were in the range 91.5-93.7%. These small differences in the amount of the absorbed water suggest that the functionalization effect does not significantly affect the porosity of most hydrogels. However, statistical post hoc comparisons of 2-ALG vs 4-ALG pair and 4-ALG vs 6-ALG pair shows that the impact of surface functionalization can play an important role (cf. Fig. S6a). Water release rates are slightly different for different hydrogels and could be attributed to different surface chemistries of the magnetic microparticles. Statistical analysis shows, however, that the observed differences are not statistically significant. During the first 8 hours of water-release the slopes of the curves are similar for all the hydrogels because the bulk concentration of microparticles in all hydrogels is only 0.9%, therefore most of the evaporating water during first hours of drying is the water absorbed in the pores of the hydrogel without direct contact with the surface of the iron microparticles. However, as the evaporation continues, more and more water molecules are in closer proximity to the functionalized surface of the microparticles. This is well seen in the last hours of drying, when some hydrogels are almost dry while others still hold water. Microparticles with primary amine groups (i.e., 1, 2) bind water more strongly than unmodified microparticles (R), or the ones modified with phenolic groups (4). This effect can be associated with various interactions of both specific (hydrogen bridges) and non-specific (electrostatic and hydrophobic interactions) character. These interactions may cause slower water release from the semi-dry hydrogel.

DSC thermograms of all tested hydrogels exhibit a broad endothermic peak starting at ~100 °C (Fig. 3b), which indicates the loss of water from the hydrogel matrix. The fastest rate of water release is

observed for R-ALG hydrogel, while for other hydrogels the dynamics of water evaporation is slower. This suggests that covering of iron particles with a silica layer, regardless of its functionalization, results in a more hydrophilic interphase in which water can be more strongly bound by the hydrophilic silica surface. Another reason may be related to differences in cross-linking of alginate, governed by various interactions of alginate chains with surface functionalities *(vide infra).* Although water evaporation peak maxima are clearly located at different temperatures, the results should be interpreted with caution as can strongly depend on the conditions of DSC experiments (Bellich, Borgogna, Carnio, & Cesàro, 2009; Craig & Reading, 2006). Nevertheless, the observed different DSC profiles (cf. Fig. 3b) confirm the water release observations of (cf. Fig. 3a), supporting the fact that water retention ability can be at least partly attributed to the effect of the presence of specific functional groups on the iron surface. In particular, the difference between hydrogels 1-ALG and 2-ALG and hydrogel 4-ALG is clearly visible. The overall conclusion can be summarized as follows: water is held more strongly by hydrogels with particles with hydrophilic surfaces (e.g. 1-ALG and 2-ALG) than by hydrogels with particles with hydrophobic surfaces (3-ALG and 5-ALG).
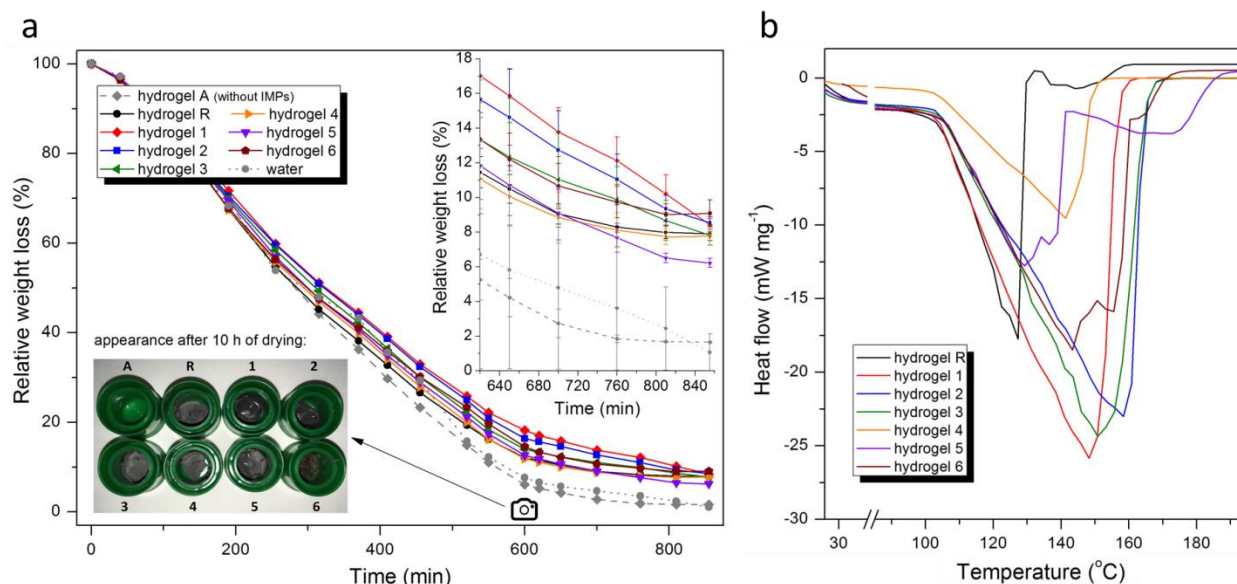
Fig. 3. (a) Water releasing kinetics upon drying (inlets: appearance of the magnetic hydrogels after 10 hours of drying (bottom), last period of drying, including error bars (top right), (b) DSC thermograms of wet magnetic hydrogels

In order to check whether the functionalization of microparticles affects the morphology of the final magnetic hydrogels, SEM imaging of selected hydrogels were run. The selected microphotographs are presented in Fig. 4 and a larger number of them is available in Supplementary. The pictures show that there are remarkable differences between ways of binding of the alginate hydrogels to the

405   microparticles surface for the considered systems. In the case of R-ALG and 4-ALG, a characteristic

406   cobweb-like network is visible which is connected only to the specific points of the surface of

407   microparticles (marked with red circles on the Fig. 4). However, most of the surface is bare due to the

408   lack of adequate surface chemistry that could ensure the appropriate interaction between alginate and

409   iron microparticles. On the other hand, in the case of 1-ALG and 2-ALG hydrogels (i.e., hydrogels with

410   abundance of amine groups on the surface), there is a completely different type of connectivity between

411   both phases. The microparticles are surrounded by a hydrogel, without significant formation of cobweb-

412   like structures but rather tight covering of most of the microparticles' surface (marked with blue circles).

413   In the case of the hydrogel 1-ALG, remarkable changes in the morphology of hydrogel chains surrounding

414   some microparticles are seen, i.e., in some places alginate chains are clearly thicker probably due to

415   strong attractive interactions between both phases.
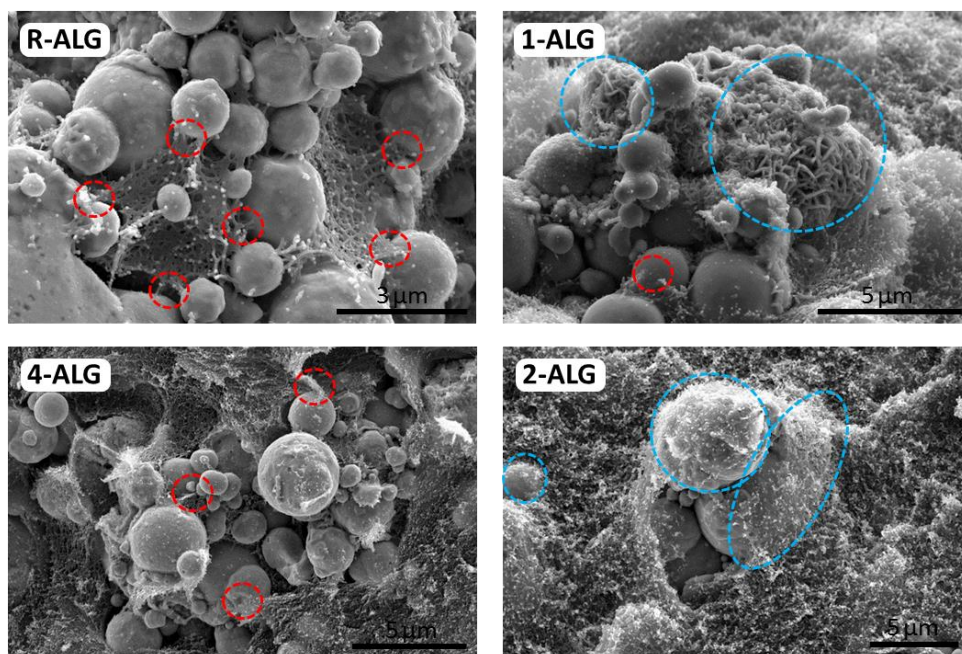
416

417   Fig. 4. SEM microphotographs of the selected hydrogels (red circles show cobweb-like single point type joints, blue circles –

418   multi point joints of the microparticles with alginate network)

419   *3.3. Quantum chemical description of possible interactions between alginate and functional groups*

420   To get more detailed view into the possible specific interactions of alginate with the surface

421   groups (particularly amine groups) DFT calculations have been carried out. Calculations of the energetic

422   effects accompanied sodium and calcium salt formation of alginic acid and comparison with those found

423   for formation of complexes with functionalities present on the microparticle surface may give an insight

424   into the competitive character of metal ions and functionalities interactions. It was found previously that

425 the effect of presence of model silica surface the functionalities are attached to is not essential to the

426 overall energetics (Barczak et al., 2018). Thus functionalities alone endcapped with hydrogen atoms were

427 considered. The relevant formulas for calculating binding energies can be also found in our earlier papers

428 (Barczak & Borowski, 2019; Barczak, Gil, Terpiłowski, Kamiński, & Borowski, 2019; Barczak et al., 2018).

429 Calculations on systems like alginic acid sodium salt $[M]_m[G]_n$ (Fig. 5a), where m and n are fairly large, are

430 impractical unless very small basis sets or semi empirical methods are used. However, in such a case the

431 calculated energetics would be highly inaccurate. The alternative is to consider the case $m=n=1$ (the MG

432 molecule) and perform the DFT calculations with extended basis set (cf. Computational details section).

433 The first problem we were faced with was endcapping of MG molecule, assumed to be a representative

434 fragment of the salt. There are two possibilities: termination with hydrogen atoms, i.e., formation of

435 hydroxyl groups, or termination with methyl groups, i.e., formation of methoxy groups. The second

436 choice (Fig. 5b) seems to be more appropriate one as in the $[M]_m[G]_n$ chain the bridging oxygen atoms

437 are bound to sp^3-hybridized carbon atom of a next unit (M or G). We believe that with such a simplified

438 model the most important interactions with Na^+, Ca^{2+}, as well as with the functionalities attached to the

439 nanoparticles will be accurately accounted for. The remaining systems representing sodium alginate

440 considered in this work for the purpose of calculating relative energies are shown in Figs 5c and 5d. The

441 representative fragment of the calcium alginate is shown in Fig. 5e. Note, that only one Ca^{2+} ion linking

442 two chains was considered in the representative fragment to reduce the overall computational cost.

443
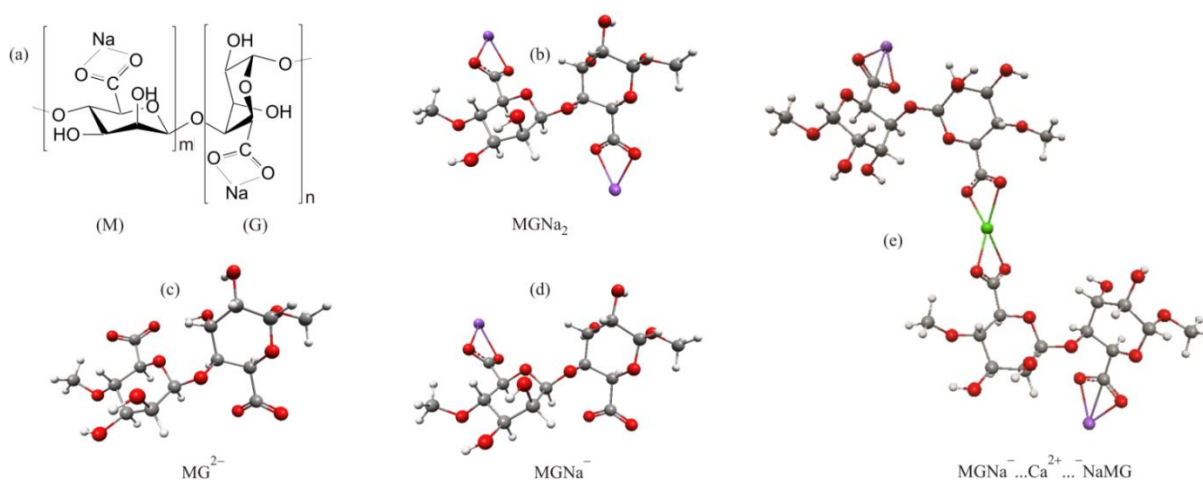
444

445 Fig. 5. (a) Sodium alginate monomer unit, (b) corresponding representative fragment endcapped with methoxy groups, MGNa$_2$,

446 (c) fully dissociated alginate unit, MG^{2-}, (d) partially dissociated alginate unit, MGNa$^-$, (e) two partially dissociated alginate units,

447 MGNa$^-$, cross-linked by Ca^{2+} cation. Colors of the atoms: grey - carbon, red - oxygen, white - hydrogen, violet - sodium, green -

448 calcium.

449

450   First the effect of dissociating of Na^+ cation from the starting model, $MGNa_2$, was investigated

451   (note that all energies are reported in kJ mol^{-1} in the reaction schemes). Dissociation of the first and then

452   second sodium cation is associated with significant overall energy increase of 1298.6 kJ mol^{-1}, i.e.,

453    $MGNa_2 \xrightarrow{+573.8} MGNa^- + Na^+$ and $MGNa^- \xrightarrow{+724.8} MG^{2-} + Na^+.$ (1)
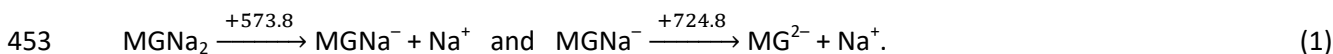
454   Such a high energy increase is associated with strong electrostatic interactions between oppositely

455   charged ions. Dissociation of $MGNa^-...Ca^{2+}...^-NaMG$ is even more energetically demanding, i.e.,

456    $MGNa^-...Ca^{2+}...^-NaMG \xrightarrow{+1991.3} 2MGNa^- + Ca^{2+}.$ (2)
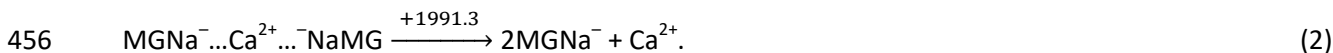
457   The binding energy of attaching the protonated amine group ($-NH_3^+$) to the carboxylic group ($-COO^-$)

458   accompanied by the formation of a complex shown in Fig. 6a is nearly -540 kJ mol^{-1},

459    $MGNa^- + {}^+H_3N-C_3H_7 \xrightarrow{-534.9} MGNa^-...^+H_3N-C_3H_7.$ (3)
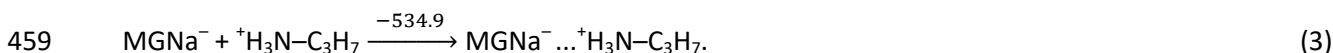
460   It thus seems that in the case of sodium alginate favorable interactions between protonated amines and

461   carboxylic groups hardly occurs as it requires additional 38.9 kJ mol^{-1} (cf. Reaction 1). The situation seems

462   to be even less advantageous in the case of calcium alginate. However, the calculated energy of a

463   process

464    $MGNa^-...Ca^{2+}...^-NaMG \xrightarrow{+549.2} MGNa^-...Ca^{2+} + MGNa^-$ (4)
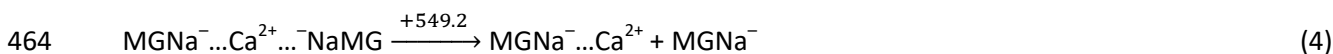
465   indicates that protonated amine groups may compete with calcium ions for carboxylic groups (this time

466   only extra 14.3 kJ mol^{-1} is required, cf. Reaction 3). On the other hand there is a number of other places

467   in the alginate monomer unit susceptible for attachment of protonated amine groups, like for example

468   structure shown in Fig. 6b. Note that protonated amine group is capable of forming two hydrogen bonds

469   with oxygen atoms present in the MG molecule: one is a bridging, and the other one is carboxylic

470   hydrogen atom. Such a double link should effectively stabilize the obtained complex. To calculate the

471   binding energies we used sodium alginate representative fragment (Fig. 5b) but the energies are not

472   expected to depend strongly on the chosen fragment. A few structures like those presented in Fig. 6b

473   were considered. All binding energies were found to be in the range from -146 to -230 kJ mol^{-1}. These

474   values are well below -80 kJ mol^{-1}, which means that the complexes are very stable at room

475   temperature. The less negative binding energy (indicating that the complex is least stable) was found for

476   the system in which the double link involves two "ether-like" oxygen atoms (e.g., bridging and hydroxyl

477   hydrogen atoms). The most negative binding energies were obtained when one of the oxygen atoms was

478   carboxylic oxygen. These energies are large enough for the complex to be very stable at room

479   temperature and follow from strong ion-dipole interactions ($U^{int} \sim r^{-2}$). It thus appears that, regardless

480   of the accessibility of carboxylic groups to functionalities present on the nanoparticle surface, alginate

481   acid salts can be successfully bound to the aminated surface of iron particles. As discussed earlier, this is

482   because the alginate chains can interact with specific functionalities also via not-carboxylic oxygen

483   arrangements, as shown in Fig. 6b.

484   More interesting is the case of protonated $-S-C{\equiv}N$ groups (denoted $-SCN^+H$). The structures

485   considered are shown in Figs 6c and d. The binding energy in a following process (Fig. 6c)

486    $$MGNa^- + H^+NCS-C_3H_7 \xrightarrow{-614.8} MGNa^-...H^+NCS-C_3H_7 \tag{5}$$
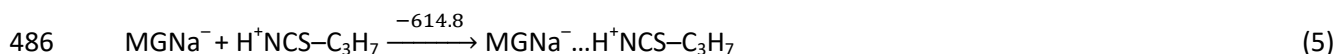
487   is high. The $-SCN^+H$ group seems to compete successfully with metal ions for the carboxylic group (cf.

488   energies reported in Reaction 1 and 4). In addition, $-SCN^+H$ group can be bound to a variety of non-

489   carboxylic oxygen atoms (similarly to the protonated amine group). One of the structures found is shown

490   in Fig. 6d and the binding energy is equal to 204.9 kJ mol^{-1}. Unfortunately the SCN-modified

491   microparticles (sample 6) are strongly corroded (cf. Figs 2 and S3) thus we could not fully verify their

492   effect on the final properties of magnetic hydrogels. However, in the case of other non-corroding

493   particles (like for example silica, titania or carbon nano/microparticles) the strong interactions predicted

494   by our calculations can be easily verified.
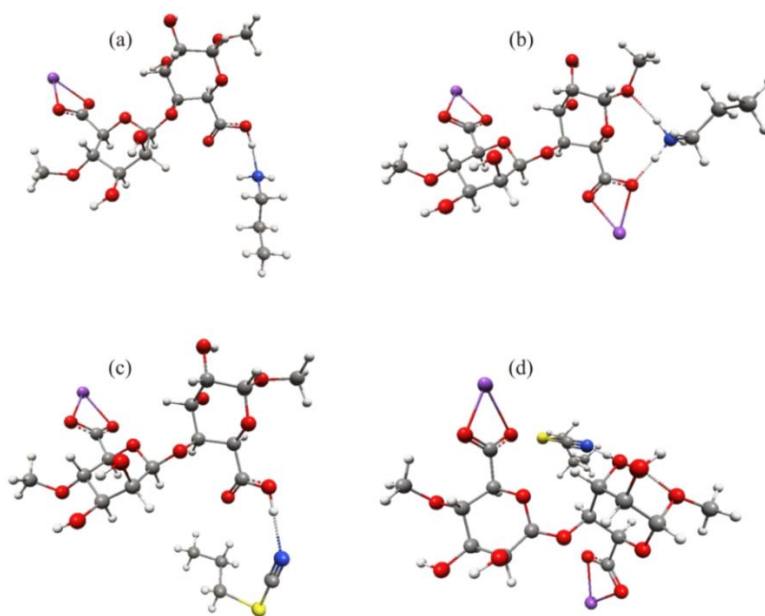
495

496   Fig. 6. (a) Complex between protonated amine group and MGNa$^-$ involving carboxylic group, (b) MGNa$_2$ doubly linked to the

497   protonated amine group, (c) complex between protonated $-S-C{\equiv}N$ group and MGNa$^-$ involving carboxylic group, (d) MGNa$_2$

498   linked to the protonated $-S-C{\equiv}N$ group through hydroxyl oxygen. Colors of the atoms: grey - carbon, red - oxygen, white -

499   hydrogen, blue - nitrogen, yellow - sulfur, violet - sodium

500

3.4. Rheological characterization of the ferrogels

502   Rheological characteristics of all the hydrogels but ALG-6 were tested using well-known protocols

503   adopted by us in our previous works. The dependence of the storage modulus (G') and loss modulus (G'')

504   as a function of the shear strain amplitude, SSA, in oscillatory regime (ν=1 Hz) is shown in Fig. S4 -as an

505   example, result for R-ALG hydrogel is shown in Fig 7a too. It has a typical shape for a viscoelastic solid-

506   like material characterized by G'>>G'' at low strain amplitude (Gila-Vilchez et al., 2018). This means that

507   the hydrogel exhibits a solid-like response. Both viscoelastic moduli have a broad plateau-like region

508   within the range of ~0.01-5 % of SSA, which is called linear viscoelastic region (LVR). When SSAs reach

509   critical values, values of G' decrease dramatically, whereas G'' first increase reaching maximum and

510   decrease afterwards. The increase in G'' represents an enhancement in the dissipation of energy related

511   to the irreversible destruction of the microstructure of the hydrogel by the shear forces. As observed in

512   Fig. S4, this maximum in G'' approximately coincides with the intersection of the curves of G' and G'',

513   with G'' being higher than G' above this maximum point, which represents a liquid-like behavior. This

514   region where G' and G'' experience rapid changes in their magnitude is known as nonlinear viscoelastic

515   region (NVR). Within this region, irreversible deformation of the internal structure of the hydrogels

516   occurs, which results in the observed decrease of elasticity manifested by huge decrease of G'. At the

517   microscopic level, these changes are explained by increasing friction between the hydrogel

518   chains/segments (increase in loss modulus, G'') as well as possible breakage of the alginate segments

519   (Cvek et al., 2020). The observed differences in G' values between hydrogels are significant for 1-ALG, 2-

520   ALG and 5-ALG hydrogels compared to R-ALG (Dunnett post hoc test, α=0.05) with p-values respectively

521   0.0001, 0.001 and 0.044. However, for 3-ALG and 4-ALG hydrogels, no significant difference was seen

522   compared to R-ALG. Detailed statistical analysis was included in Supplementary data (cf. Fig. S6b).

523   Looking at these values collected in Table 2 (and also, for better visualization in Fig. 7c) it can be

524   seen that the incorporation of amine-modified microparticles 1 and 2 results in much higher values of G'

525   of the resulting hydrogels 1-ALG and 2-ALG (410 and 483 Pa, respectively) when compared with the

526   hydrogel R-ALG (137 Pa). In contrast, hydrogels doped with glycidoxy- and phenyl-functionalized IMPs (3

527   and 4, respectively) have almost non-affected G' values (112 and 141 Pa, respectively). These results

528   agree with the differences in adhesion between polymer chains and particles observed by means of

529   electron microscopy (Fig. 4), and clearly demonstrate the critical role of the proper functionalization of

530   the iron particles in governing final mechanical properties of the resulting hydrogels. Another

531   characteristic feature is the maximum in G'' modulus that is known as yielding point, at which dissipation

532   of energy is maximal (Moghimi, Jacob, Koumakis, & Petekidis, 2017). The values of SSA corresponding to

533   the maximal values of G" are also collected in Table 2. Differences between them can be also attributed

534   to the changes of the structure of hydrogels due to different interactions with various microparticles.

535   Table 2. Mean values of G' corresponding to the LVR and values of SSA in yielding point for the hydrogels studied

	No magnetic field		Magnetic field: 141 kA m^{-1}		Magnetic field: 282 kA m^{-1}	
hydrogel	G'_{LVR}	SSA of G''_{max}	G'_{LVR}	SSA of G''_{max}	G'_{LVR}	SSA of G''_{max}
	(Pa)	(%)	(Pa)	(%)	(Pa)	(%)
R-ALG	137±34	5-26	1278±151	72	2088±202	36
1-ALG	410±105	18	1429±243	43	2117±338	36
2-ALG	483±83	22	1600±33	51	2267±75	43
3-ALG	112±22	13-72	1486±357	51	2297±441	31
4-ALG	141±24	16	1223±250	43	1982±373	36
5-ALG	286±58	13-36	1152±404	43	1660±661	31

536
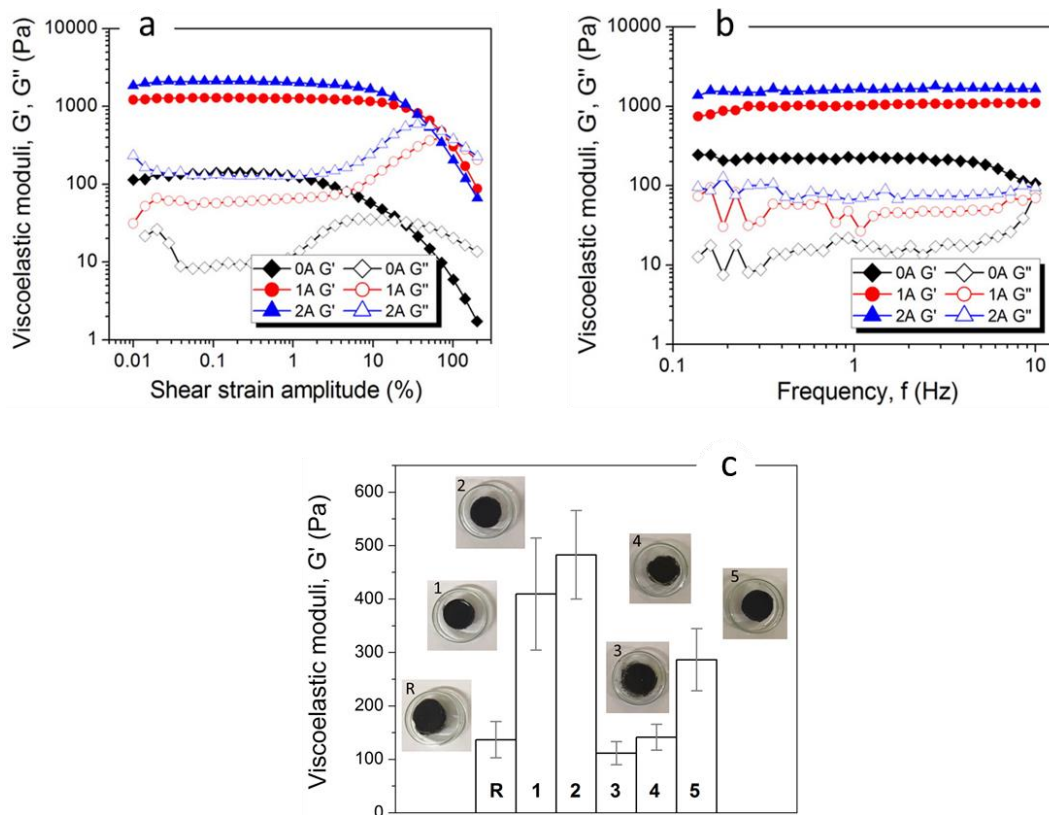
537

538   Fig. 7. (a) Storage and loss moduli of the R-ALG hydrogel as a function of shear strain amplitude. (b) Storage and loss moduli of

539   R-ALG hydrogel as a function of frequency. 0A refers to the measurements without the presence of magnetic field, 1A and 2A

540   refer to the magnetic field of 141 kA m-1 and 242 kA m-1, respectively. (c) Comparison of the values of storage modulus (G') of

541   the hydrogels studied without the presence of magnetic field

542   In the presence of the magnetic field strong increase of the viscoelastic moduli is observed due to

543   the magnetically induced reorganization of the structure, which was not hindered by the elastic matrix of

544   alginate hydrogel. Furthermore, as observed in Fig. S4 and Table 2 (see also Fig. 7a for R-ALG hydrogel),

545   in the presence of applied magnetic field the onset of the NVR and the yielding point move in general to

546   higher values of the SSA, with respect to the absence of applied field, something that must be connected

547   to the strengthening of the microstructure due to the interparticle attraction mediated by the applied

548   magnetic field. The magnetic field-dependence for all the magnetic hydrogels is similar.

549   The dependence of both viscoelastic moduli as a function of frequency within the LVR was also

550   analyzed and is presented in Fig. S5 (as an example, result for R-ALG hydrogel is shown in Fig 7b too). As

551   observed, both moduli, G' and G", only slightly change with the frequency of oscillation for the range of

552   frequencies under study (0.1-10 Hz). In all cases G' was considerably larger than G". The observed

553   tendencies are typical of cross-linked polymer systems (Macosko, 1994), as well as of soft human tissues

554   (Callejas et al., 2017). As expected, the values of G' and G" remarkably increases when magnetic field is

555   applied during rheological measurements.

556

557   *3.5. Assessment of cell viability*

558   Finally, cell viability of the selected hydrogels has been tested. At this point it should be mentioned

559   that we wanted merely to compare the selected hydrogels (i.e., R-ALG, 2-ALG and 4-ALG) with each

560   other rather than to assess absolute cytotoxicity. This is due to the fact that a thorough cytotoxicological

561   study would require finding interrelations between the cell viability and alginate concentration, cell

562   density, calcium concentration and exposing time. For example, it was reported that exposure of cells to

563   the calcium environment (note that calcium ions are involved in crosslinking process) can cause

564   significant loss of living cells in culture media (Cao, Chen, & Schreyer, 2012). Such as rigorous study was

565   not the aim of this work. Representative fluorescence micrographs of calcein-AM-stained, live cells

566   (green) and propidium iodide-stained, dead cells (red), corresponding to the Live/Dead assay are shown

567   in Fig. 8a. As can be seen, the number of live cells was significantly reduced for all alginate magnetic

568   hydrogels studied when compared with the control cells. Most importantly, we observed differences

569   between the tested hydrogels: in the case of R-ALG sample, no dead cells were observed on the top of

570   the hydrogel, while in the case of 4-ALG sample, a significant number of dead cells was found on some

571   images. Statistical analysis of the functional WST-1 assays (Fig. 8b) showed significant differences among

572   hydrogels R-ALG and 4-ALG (p-value<0.0001) but not R-ALG and 2-ALG (p-value=0.016). This means that

573   amine groups present on the surface of the sample 2 does not results in decreased cell viability. In

23

contrast, functionalization with phenyl groups (sample 4) makes the resulting hydrogel less biocompatible. Therefore, it can be concluded that biocompatibility of the hydrogels depends on the surface chemistry of functionalized microparticles and thus, apart from the macroscopic and mechanical properties, also the cell viability depends on the functionalization (cf. Fig. S6c). These results are confirmed by the free DNA quantification analysis showing statistically significant differences between all the compared samples (cf. Fig. S6d). As it can be seen from the Fig. 8c, 4-ALG hydrogel was associated with the highest levels of cell damage and DNA release to the culture medium, while the hydrogels R-ALG and 2-ALG showed much better biocompatibility.
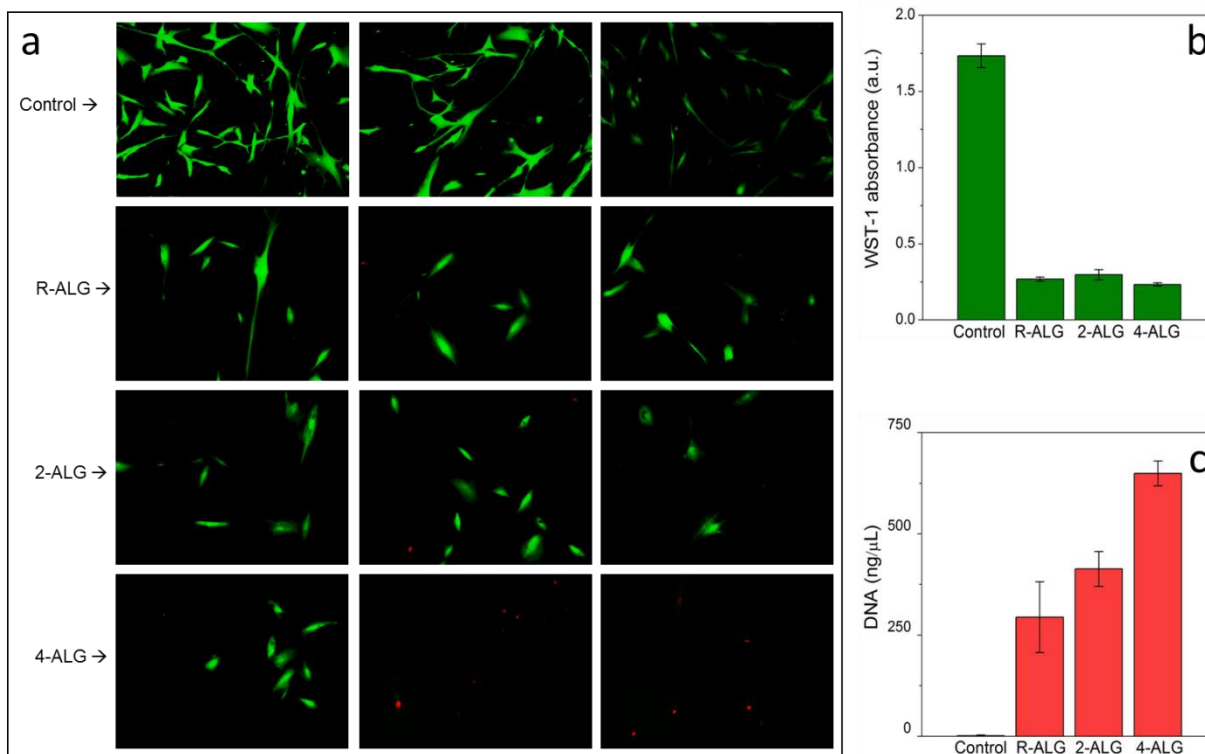
Fig. 8. (a) Cytotoxicity of the selected hydrogels revealed by the fluorescence microscopy, (b) WST-1 absorbance test, (c) and DNA quantification in the cell medium

4. Conclusions

Iron microparticles were modified by introducing a number of functionalities on their surface, ranging from amine to phenyl groups. Although surface functionalizations have not significantly affected the properties of the microparticles themselves, they changed remarkably the final properties of magnetic hydrogels obtained by embedding the iron microparticles into the pre-polymerized alginate matrix. Thus, the successful dispersion of functionalized microparticles was twofold beneficial: (i) magnetic activity

24

592   was introduced *in-situ*, (ii) enhancement of the macroscopic and mechanical properties was achieved

593   thanks to the altered interactions of alginate with functionalized surface. Among all the systems studied,

594   amine functionalized IMP-based hydrogels exhibited superior properties when compared with the

595   hydrogel prepared with the use of their non-functionalized counterpart. Properties such as hydrogel

596   integrity, water-holding capability, storage modulus of the amine-based hydrogels of 2-ALG and 4-ALG

597   were significantly altered in comparison with R-ALG hydrogel. For example, storage moduli for the

598   former ones are 410 and 483 Pa, respectively, while for the latter - only 137 Pa. SEM images revealed

599   that the lack of adequate surface chemistry limits the contact between both phases, which are

600   connected only by limited number of anchoring points. In contrast, amination of the iron surface results

601   in more tight covering of most of the microparticles' surface by multiple connections. Theoretical DFT

602   calculations revealed that alginate chains are chemically active not only because of the presence of

603   carboxyl groups but also other non-carboxylic oxygen arrangements which can interact with

604   functionalities. Even blocking of all carboxyl groups by calcium cations during alginate crosslinking does

605   not limit the possibility of tuning of alginate interactions with appropriately modified surfaces.

606

613

614

615   **Literature**

616   Anderson, T. F. (1951). Techniques for the preservation of three-dimensional structure in preparing

617   specimens for the electron microscope. *New York Academy of Sciences. Transactions*, *13*, 130–134.

618   Baker, J., Wolinski, K., Malagoli, M., Kinghorn, D., Wolinski, P., Magyarfalvi, G., … Pulay, P. (2009).

619   Quantum chemistry in parallel with PQS. *Journal of Computational Chemistry*, *30*(2), 317–335.

620   https://doi.org/10.1002/jcc.21052

621   Barbucci, R., Giani, G., Fedi, S., Bottari, S., & Casolaro, M. (2012). Biohydrogels with magnetic

622   nanoparticles as crosslinker: Characteristics and potential use for controlled antitumor drug-

delivery. *Acta Biomaterialia*, *8*(12), 4244–4252. https://doi.org/10.1016/J.ACTBIO.2012.09.006

Barczak, M., & Borowski, P. (2019). Silica xerogels modified with amine groups: Influence of synthesis

    parameters on porous structure and sorption properties. *Microporous and Mesoporous Materials*,

    281, 32–43. https://doi.org/10.1016/J.MICROMESO.2019.02.032

Barczak, M., Gil, M., Terpiłowski, K., Kamiński, D., & Borowski, P. (2019). Influence of bridged monomer

    on porosity and sorption properties of mesoporous silicas functionalized with diethylenetriamine

    groups. *Adsorption*, *25*(3), 575–589. https://doi.org/10.1007/s10450-019-00047-z

Barczak, M., Wierzbicka, M., & Borowski, P. (2018). Sorption of diclofenac onto functionalized

    mesoporous silicas: Experimental and theoretical investigations. *Microporous and Mesoporous*

    Materials, *264*, 254–264. https://doi.org/10.1016/J.MICROMESO.2018.01.013

Bellich, B., Borgogna, M., Carnio, D., & Cesàro, A. (2009). Thermal behavior of water in micro-particles

    based on alginate gel. In *Journal of Thermal Analysis and Calorimetry* (Vol. 97, pp. 871–878).

    Springer. https://doi.org/10.1007/s10973-009-0392-x

Bonhome-Espinosa, A. B., Campos, F., Rodriguez, I. A., Carriel, V., Marins, J. A., Zubarev, A., … Lopez-

    Lopez, M. T. (2017). Effect of particle concentration on the microstructural and macromechanical

    properties of biocompatible magnetic hydrogels. *Soft Matter*, *13*(16), 2928–2941.

    https://doi.org/10.1039/C7SM00388A

Brochier Salon, M.-C., & Belgacem, M. N. (2011). Hydrolysis-Condensation Kinetics of Different Silane

    Coupling Agents. *Phosphorus, Sulfur, and Silicon and the Related Elements*, *186*(2), 240–254.

    https://doi.org/10.1080/10426507.2010.494644

Buenger, D., Topuz, F., & Groll, J. (2012). Hydrogels in sensing applications. *Progress in Polymer Science*,

    37(12), 1678–1719. https://doi.org/10.1016/J.PROGPOLYMSCI.2012.09.001

Burrell, M. C. (2001). Chemical Analysis, Electron Spectroscopy. *Encyclopedia of Materials: Science and*

    Technology, 1142–1149. https://doi.org/10.1016/B0-08-043152-6/00214-X

Callejas, A., Gomez, A., Melchor, J., Riveiro, M., Massó, P., Torres, J., … Rus, G. (2017). Performance study

    of a torsional wave sensor and cervical tissue characterization. *Sensors (Switzerland)*, *17*(9).

    https://doi.org/10.3390/s17092078

Čampelj, S., Makovec, D., & Drofenik, M. (2009). Functionalization of magnetic nanoparticles with 3-

    aminopropyl silane. *Journal of Magnetism and Magnetic Materials*, *321*(10), 1346–1350.

    https://doi.org/10.1016/j.jmmm.2009.02.036

Cao, N., Chen, X. B., & Schreyer, D. J. (2012). Influence of Calcium Ions on Cell Survival and Proliferation

    in the Context of an Alginate Hydrogel. *International Scholarly Research Network ISRN Chemical*

655 *Engineering*, *2012*. https://doi.org/10.5402/2012/516461

656 Censi, R., Gigliobianco, M. R., Malaj, L., & Di Martino, P. (2016). Effect of poly(vinylpyrrolidone) or sodium

657 alginate on the stability of the amorphous form of nimesulide. *Journal of Thermal Analysis and*

658 *Calorimetry*, *123*(3), 2415–2425. https://doi.org/10.1007/s10973-015-5175-y

659 Craig, D. Q. M., & Reading, M. (2006). *Thermal Analysis of Pharmaceuticals*. *Thermal Analysis of*

660 *Pharmaceuticals*. CRC Press. https://doi.org/10.1201/9781420014891

661 Cvek, M., Zahoranova, A., Mrlik, M., Sramkova, P., Minarik, A., & Sedlacik, M. (2020). Poly(2-oxazoline)-

662 based magnetic hydrogels: Synthesis, performance and cytotoxicity. *Colloids and Surfaces B:*

663 *Biointerfaces*, *190*, 110912. https://doi.org/10.1016/j.colsurfb.2020.110912

664 De Groot, C. J., Van Luyn, M. J. ., Van Dijk-Wolthuis, W. N. ., Cadée, J. A., Plantinga, J. A., Otter, W. Den, &

665 Hennink, W. E. (2001). In vitro biocompatibility of biodegradable dextran-based hydrogels tested

666 with human fibroblasts. *Biomaterials*, *22*(11), 1197–1203. https://doi.org/10.1016/S0142-

667 9612(00)00266-0

668 Dimatteo, R., Darling, N. J., & Segura, T. (2018). In situ forming injectable hydrogels for drug delivery and

669 wound repair. *Advanced Drug Delivery Reviews*, *127*, 167–184.

670 https://doi.org/10.1016/J.ADDR.2018.03.007

671 Donati, I., Gamini, A., Skjåk-Bræk, G., Vetere, A., Campa, C., Coslovi, A., & Paoletti, S. (2003).

672 Determination of the diadic composition of alginate by means of circular dichroism: A fast and

673 accurate improved method. *Carbohydrate Research*, *338*(10), 1139–1142.

674 https://doi.org/10.1016/S0008-6215(03)00094-6

675 Drury, J. L., & Mooney, D. J. (2003). Hydrogels for tissue engineering: scaffold design variables and

676 applications. *Biomaterials*, *24*(24), 4337–4351. https://doi.org/10.1016/S0142-9612(03)00340-5

677 Du, X., Zhou, J., Shi, J., & Xu, B. Supramolecular Hydrogelators and Hydrogels: From Soft Matter to

678 Molecular Biomaterials, 115 Chemical Reviews § (2015). American Chemical Society. Retrieved from

679 https://pubs.acs.org/doi/10.1021/acs.chemrev.5b00299

680 Espona-Noguera, A., Ciriza, J., Cañibano-Hernández, A., Fernandez, L., Ochoa, I., Saenz del Burgo, L., &

681 Pedraz, J. L. (2018). Tunable injectable alginate-based hydrogel for cell therapy in Type 1 Diabetes

682 Mellitus. *International Journal of Biological Macromolecules*, *107*, 1261–1269.

683 https://doi.org/10.1016/J.IJBIOMAC.2017.09.103

684 Fan, D., Tian, Y., & Liu, Z. (2019). Injectable Hydrogels for Localized Cancer Therapy. *Frontiers in*

685 *Chemistry*, *7*, 675. https://doi.org/10.3389/fchem.2019.00675

686 Filippov, M. P., & Kohn, R. (1974). Determination of composition of alginates by infrared spectroscopic

687   method. *Chemicke Zvesti*, *28*(6), 817–819.

688   Fitzpatrick, S. E., Staiger, M. P., Deb-Choudhury, S., & Ranford, S. (2018). Protein-based Aerogels:

689   Processing and Morphology. In *RSC Green Chemistry* (Vol. 2018-Janua, pp. 67–102). Royal Society of

690   Chemistry. https://doi.org/10.1039/9781782629979-00067

691   Geckil, H., Xu, F., Zhang, X., Moon, S., & Demirci, U. (2010). Engineering hydrogels as extracellular matrix

692   mimics. *Nanomedicine*, *5*(3), 469–484. https://doi.org/10.2217/nnm.10.12

693   Giani, G., Fedi, S., & Barbucci, R. (2012). Hybrid Magnetic Hydrogel: A Potential System for Controlled

694   Drug Delivery by Means of Alternating Magnetic Fields. *Polymers*, *4*(2), 1157–1169.

695   https://doi.org/10.3390/polym4021157

696   Gila-Vilchez, C., Bonhome-Espinosa, A. B., Kuzhir, P., Zubarev, A., Duran, J. D. G., & Lopez-Lopez, M. T.

697   (2018). Rheology of magnetic alginate hydrogels. *Journal of Rheology*, *62*(5), 1083–1096.

698   https://doi.org/10.1122/1.5028137

699   Gila-Vilchez, C., Duran, J. D. G., Gonzalez-Caballero, F., Zubarev, A., & Lopez-Lopez, M. T. (2019).

700   Magnetorheology of alginate ferrogels. *Smart Materials and Structures*, *28*(3), 035018.

701   https://doi.org/10.1088/1361-665X/aafeac

702   Gila-Vilchez, C., Mañas-Torres, M. C., Contreras-Montoya, R., Alaminos, M., Duran, J. D. G., de

703   Cienfuegos, L. Á., & Lopez-Lopez, M. T. (2019). Anisotropic magnetic hydrogels: design, structure

704   and mechanical properties. *Philosophical Transactions of the Royal Society A: Mathematical,*

705   *Physical and Engineering Sciences*, *377*(2143), 20180217. https://doi.org/10.1098/rsta.2018.0217

706   Griffin, D. R., Weaver, W. M., Scumpia, P. O., Di Carlo, D., & Segura, T. (2015). Accelerated wound healing

707   by injectable microporous gel scaffolds assembled from annealed building blocks. *Nature Materials*,

708   *14*(7), 737–744. https://doi.org/10.1038/nmat4294

709   Konwar, A., Gogoi, A., & Chowdhury, D. (2015). Magnetic alginate–Fe_3O_4 hydrogel fiber capable of

710   ciprofloxacin hydrochloride adsorption/separation in aqueous solution. *RSC Advances*, *5*(99),

711   81573–81582. https://doi.org/10.1039/C5RA16404D

712   Kulkarni, R. V., Boppana, R., Krishna Mohan, G., Mutalik, S., & Kalyane, N. V. (2012). pH-responsive

713   interpenetrating network hydrogel beads of poly(acrylamide)-g-carrageenan and sodium alginate

714   for intestinal targeted drug delivery: Synthesis, in vitro and in vivo evaluation. *Journal of Colloid and*

715   *Interface Science*, *367*(1), 509–517. https://doi.org/10.1016/j.jcis.2011.10.025

716   Lai, J.-Y. (2010). Biocompatibility of chemically cross-linked gelatin hydrogels for ophthalmic use. *Journal*

717   *of Materials Science: Materials in Medicine*, *21*(6), 1899–1911. https://doi.org/10.1007/s10856-

718   010-4035-3

719   Lee, C., Shin, J., Lee, J. S., Byun, E., Ryu, J. H., Um, S. H., … Cho, S.-W. (2013). Bioinspired, Calcium-Free

720   Alginate Hydrogels with Tunable Physical and Mechanical Properties and Improved

721   Biocompatibility. *Biomacromolecules*, *14*(6), 2004–2013. https://doi.org/10.1021/bm400352d

722   Lee, K. Y., & Mooney, D. J. (2012). Alginate: Properties and biomedical applications. *Progress in Polymer*

723   *Science*, *37*(1), 106–126. https://doi.org/10.1016/J.PROGPOLYMSCI.2011.06.003

724   Li, J., & Mooney, D. J. (2016). Designing hydrogels for controlled drug delivery. *Nature Reviews Materials*,

725   *1*(12), 16071. https://doi.org/10.1038/natrevmats.2016.71

726   Li, L., Wang, Y., Pan, L., Shi, Y., Cheng, W., Shi, Y., & Yu, G. (2015). A Nanostructured Conductive

727   Hydrogels-Based Biosensor Platform for Human Metabolite Detection. *Nano Letters*, *15*(2), 1146–

728   1151. https://doi.org/10.1021/nl504217p

729   Li, X., Sun, Q., Li, Q., Kawazoe, N., & Chen, G. (2018). Functional Hydrogels With Tunable Structures and

730   Properties for Tissue Engineering Applications. *Frontiers in Chemistry*, *6*, 499.

731   https://doi.org/10.3389/fchem.2018.00499

732   Liu, S., & Guo, W. (2018). Anti-Biofouling and Healable Materials: Preparation, Mechanisms, and

733   Biomedical Applications. *Advanced Functional Materials*, *28*(41), 1800596.

734   https://doi.org/10.1002/adfm.201800596

735   Long, J., Li, X., Wu, Z., Xu, E., Xu, X., Jin, Z., & Jiao, A. (2015). Immobilization of pullulanase onto activated

736   magnetic chitosan/Fe3O4 nanoparticles prepared by in situ mineralization and effect of surface

737   functional groups on the stability. *Colloids and Surfaces A: Physicochemical and Engineering*

738   *Aspects*, *472*, 69–77. https://doi.org/10.1016/J.COLSURFA.2015.02.038

739   Macosko, C. W. (1994). *Rheology: Principles, Measurements, and Applications ABOUT THE AUTHOR*.

740   Wiley-VCH. Retrieved from https://www.wiley.com/en-us

741   Mahinroosta, M., Jomeh Farsangi, Z., Allahverdi, A., & Shakoori, Z. (2018). Hydrogels as intelligent

742   materials: A brief review of synthesis, properties and applications. *Materials Today Chemistry*, *8*,

743   42–55. https://doi.org/10.1016/J.MTCHEM.2018.02.004

744   Mantha, S., Pillai, S., Khayambashi, P., Upadhyay, A., Zhang, Y., Tao, O., … Tran, S. D. (2019). Smart

745   Hydrogels in Tissue Engineering and Regenerative Medicine. *Materials*, *12*(20), 3323.

746   https://doi.org/10.3390/ma12203323

747   Marcus, M., Skaat, H., Alon, N., Margel, S., & Shefi, O. (2015). NGF-conjugated iron oxide nanoparticles

748   promote differentiation and outgrowth of PC12 cells. *Nanoscale*, *7*(3), 1058–1066.

749   https://doi.org/10.1039/C4NR05193A

750   Melendres, C. A., O'Leary, T. J., & Solis, J. (1991). Effect of thiocyanate on the corrosion and passivation

751   behaviour of copper and iron: laser Raman spectroscopy and photoelectrochemical studies.

752   *Electrochimica Acta*, *36*(3–4), 505–511. https://doi.org/10.1016/0013-4686(91)85134-S

753   Moghimi, E., Jacob, A. R., Koumakis, N., & Petekidis, G. (2017). Colloidal gels tuned by oscillatory shear.

754   *Soft Matter*, *13*(12), 2371–2383. https://doi.org/10.1039/c6sm02508k

755   Morris, E. R., Rees, D. A., & Thom, D. (1980). Characterisation of alginate composition and block-

756   structure by circular dichroism. *Carbohydrate Research*, *81*(2), 305–314.

757   https://doi.org/10.1016/S0008-6215(00)85661-X

758   Osterholtz, F. D., & Pohl, E. R. (1992). Kinetics of the Hydrolysis and Condensation of Organofunctional

759   Alkoxysilanes: A Review. *Journal of Adhesion Science and Technology*, *6*(1), 127–149.

760   https://doi.org/10.1163/156856192X00106

761   Park, S., Lee, Y., Kim, D. N., Park, S., Jang, E., & Koh, W.-G. (2009). Entrapment of enzyme-linked magnetic

762   nanoparticles within poly(ethylene glycol) hydrogel microparticles prepared by photopatterning.

763   *Reactive and Functional Polymers*, *69*(5), 293–299.

764   https://doi.org/10.1016/J.REACTFUNCTPOLYM.2009.02.001

765   Peppas, N. A., Hilt, J. Z., Khademhosseini, A., & Langer, R. (2006). Hydrogels in Biology and Medicine:

766   From Molecular Principles to Bionanotechnology. *Advanced Materials*, *18*(11), 1345–1360.

767   https://doi.org/10.1002/adma.200501612

768   Prencipe, I., Dellasega, D., Zani, A., Rizzo, D., & Passoni, M. (2015). Energy dispersive x-ray spectroscopy

769   for nanostructured thin film density evaluation. *Science and Technology of Advanced Materials*,

770   *16*(2), 025007. https://doi.org/10.1088/1468-6996/16/2/025007

771   Qiu, Y., & Park, K. Environment-sensitive hydrogels for drug delivery. *Advanced Drug Delivery Reviews*,

772   (3). Retrieved from

773   https://www.sciencedirect.com/science/article/pii/S0169409X01002034?via%3Dihub

774   Qureshi, D., Nayak, S. K., Maji, S., Anis, A., Kim, D., & Pal, K. (2019). Environment sensitive hydrogels for

775   drug delivery applications. *European Polymer Journal*, *120*, 109220.

776   https://doi.org/10.1016/J.EURPOLYMJ.2019.109220

777   Ravald, L. A., Chilver, J. W., & Williams, R. (2007). The corrosion of mild steel by aqueous ammonium

778   thiocyanate. *Journal of Applied Chemistry*, *7*(3), 113–117. https://doi.org/10.1002/jctb.5010070304

779   Seliktar, D. (2012). Designing cell-compatible hydrogels for biomedical applications. *Science (New York,*

780   *N.Y.)*, *336*(6085), 1124–1128. https://doi.org/10.1126/science.1214804

781   Soon-Shiong, P., Heintz, R. E., Merideth, N., Yao, Q. X., Yao, Z., Zheng, T., … Sandford, P. A. (1994). Insulin

782   independence in a type 1 diabetic patient after encapsulated islet transplantation. *The Lancet*,

343(8903), 950–951. https://doi.org/10.1016/S0140-6736(94)90067-1

Supramaniam, J., Adnan, R., Mohd Kaus, N. H., & Bushra, R. (2018). Magnetic nanocellulose alginate hydrogel beads as potential drug delivery system. *International Journal of Biological Macromolecules*, *118*, 640–648. https://doi.org/10.1016/J.IJBIOMAC.2018.06.043

Tanasa, E., Zaharia, C., Radu, I.-C., Surdu, V.-A., Vasile, B. S., Damian, C.-M., & Andronescu, E. (2019). Novel Nanocomposites Based on Functionalized Magnetic Nanoparticles and Polyacrylamide: Preparation and Complex Characterization. *Nanomaterials*, *9*(10), 1384. https://doi.org/10.3390/nano9101384

Tu, Y., Chen, N., Li, C., Liu, H., Zhu, R., Chen, S., … He, L. (2019). Advances in injectable self-healing biomedical hydrogels. *Acta Biomaterialia*, *90*, 1–20. https://doi.org/10.1016/J.ACTBIO.2019.03.057

Ulijn, R. V., Bibi, N., Jayawarna, V., Thornton, P. D., Todd, S. J., Mart, R. J., … Gough, J. E. (2007). Bioresponsive hydrogels. *Materials Today*, *10*(4), 40–48. https://doi.org/10.1016/S1369-7021(07)70049-4

Wang, H., Jiang, L., Wu, H., Zheng, W., Kan, D., Cheng, R., … Sun, S.-K. (2019). Biocompatible Iodine–Starch–Alginate Hydrogel for Tumor Photothermal Therapy. *ACS Biomaterials Science & Engineering*, *5*(7), 3654–3662. https://doi.org/10.1021/acsbiomaterials.9b00280

Zhu, Y., Zheng, Y., Wang, F., & Wang, A. (2016). Fabrication of magnetic macroporous chitosan-g-poly (acrylic acid) hydrogel for removal of Cd2+ and Pb2+. *International Journal of Biological Macromolecules*, *93*, 483–492. https://doi.org/10.1016/J.IJBIOMAC.2016.09.005